RSC Advances

PAPER

View Article Online
View Journal | View Issue

Cite this: *RSC Adv.*, 2024, **14**, 38391

Novel feathery P/S Co-doped graphitic carbon nitride for highly efficient synergistic photocatalytic H_2O_2 generation and tetracycline degradation†

Lian Qin,[a] Zhongli Zhao,[a] Ning Fu,[a] Xiangyu Li,[a] Lei Hu,[b] Xingang Li[c] and Chun Zhang*[a]

Graphitic carbon nitride (g-C_3N_4) has garnered significant attention in photocatalytic pollutant degradation for its non-toxicity and cost-effectiveness. However, its limited photocatalytic performance has hindered its applications. Addressing this, we successfully synthesized a novel feathery multifunctional catalyst, phosphorus and sulfur co-doped g-C_3N_4 ($P_{0.3}S_{0.2}$-CN), with an enlarged pore network through a hydrothermal method. This catalyst exhibits remarkable photocatalytic performance under visible light, achieving a hydrogen peroxide (H_2O_2) production rate of 28.6 mg L^{-1} h^{-1} and an efficiency of 87.3% in degrading tetracycline (TC). Comparative studies demonstrate that $P_{0.3}S_{0.2}$-CN outperforms singly doped catalysts $P_{0.5}$-CN and $S_{0.4}$-CN by increasing H_2O_2 yield by 28.67% and 53.28% and improving TC degradation by 15.2% and 11.5%, respectively. These improvements can be attributed to the synergetic effects of P and S co-doping and the high number of active sites provided by its peculiar morphology, which enhance charge transfer and photocatalytic activity, and a more pronounced conjugation effect, resulting in a high electrostatic potential surface conducive to adsorption and activation, as confirmed by density-functional theory calculations. Our findings propose a mechanism for the synergistic photocatalytic-Fenton degradation (PSF) of TC using $P_{0.3}S_{0.2}$-CN. This present research contributes to the advancement of g-C_3N_4-based photocatalysts and promotes the exploration of more efficient carbon-based catalysts for environmental remediation.

Received 13th August 2024
Accepted 21st September 2024

DOI: 10.1039/d4ra05879h

rsc.li/rsc-advances

1. Introduction

The rapid development of industry and agriculture has inevitably resulted in a series of environmental issues, with various types of domestic sewage, industrial and agricultural wastewater, industrial soot, and automobile exhausts releasing harmful substances into the environment. Among these pollutants, antibiotics present in natural water sources poses a serious threat to both the ecological cycle and human health.[1] Antibiotics are typically characterized by their high stability and resistance to biodegradation. Besides, traditional physical and chemical treatment methods may lead to secondary toxic contamination and generally require a long duration (at least 3 months). Moreover, the removal efficiency of physical-chemical treatment is usually insignificant, greatly limiting its application for organic pollutants. Tetracycline, one of the broad-spectrum antibiotics containing acylamino groups, dimethylamino groups, phenolic hydroxyl groups, and ketoenol conjugated double bonds, is extensively consumed and produced in China.[2] Therefore, it is crucial to develop clean degradation methods that are free from secondary pollution and environmentally friendly. Advanced oxidation processes (AOPs) offer an excellent solution for oxidizing and mineralizing toxic and refractory organics in complex wastewater treatment compared to other conventional approaches.[3,4] The main challenges associated with homogeneous Fenton systems include (1) high consumption cost of H_2O_2, (2) limited pH adaptability (pH ≤ 3), and (3) the low cyclic conversion rate of Fe^{3+}/Fe^{2+}.[5–8] Interestingly, *in situ* generation and consumption of H_2O_2 within the Fenton system can effectively address these concerns related to costliness and safety risk.[9] Therefore, the development of an *in situ* self-Fenton system is imperative for the efficient elimination of TC from the aqueous environment.

The photocatalytic oxygen reduction reaction has emerged as a sustainable approach for the production of H_2O_2,[10] offering significant advantages in terms of cost-effectiveness,

[a]*School of Chemistry and Chemical Engineering, Lanzhou Jiaotong University, Lanzhou 730070, PR China. E-mail: zh-chun@163.com*

[b]*Chongqing Titanium Industry Co. Ltd of Pangang Group, Chongqing 400055, PR China*

[c]*Laboratory of Applied Catalysis Science and Engineering, Tianjin University, Tianjin 300072, PR China*

† Electronic supplementary information (ESI) available. See DOI: https://doi.org/10.1039/d4ra05879h

environmental friendliness, safety and efficiency. The construction of PSF systems may also serve as an effective method for the degradation of TC.[11,12] For instance, the CdS/rGO/Fe^{2+} composite in a PSF system achieved efficient degradation of various organic compounds by generating H_2O_2 *in situ*, exemplifying its effectiveness.[13] However, limitations in the application of sulfides arise from their inherent instability and biotoxicity. In recent years, g-C_3N_4 materials have gained significant traction in the optoelectronics field due to their favorable energy band position, exceptional chemical stability, and cost-effectiveness.[14,15] Nevertheless, the photocatalytic performance of g-C_3N_4 is greatly limited by its rapid carrier complexation and small specific surface area.[16–20] Fortunately, the photocatalytic activity and efficiency of g-C_3N_4 can be enhanced through nanostructure engineering, ion doping, and the formation of composite materials. The desired morphology can be achieved through the process of hard template synthesis. However, during the removal of the template, nanocrystallinity inevitably appears as structural defects, which can be effectively addressed by employing self-assembly techniques. The supramolecular self-assembly process enables the formation of specialized nanostructures, including nanoribbons,[21] nanorods,[22] nanotubes[23] and nanoflakes.[24] These structures exhibit enhanced specific surface area and light absorption capacity, thereby facilitating superior light scattering ability, increased light utilization efficiency, larger specific surface area, and greater exposure of active sites.

The improvement of g-C_3N_4 materials for efficient photocatalysis through a single strategy may pose challenges, while elemental doping has been demonstrated as an effective approach to modulate both the photoelectric and chemical properties of g-C_3N_4.[25–27] The heteroatom doping of g-C_3N_4 involves a robust coordination between carbon and nitrogen atoms, as well as other atoms, which benefits the delocalization of π-conjugated electrons for effective charge separation and modulation of the energy band structure.[28–30] Theoretical studies based on first principles have shown a preferential substitution of S and P atoms for N and C atoms specifically at the edges of g-C_3N_4 within the gaps located at angular sites.[31] Theoretical calculations revealed enhanced photocatalytic activity and stability in the sulfur-doped g-C_3N_4 (S_y-CN) heptazine-based framework.[32] The presence of P-doped g-C_3N_4 (P_x-CN) nanoribbons can effectively suppress the aggregation between NH_2 groups, thereby promoting the degradation and hydrogenation of pollutants.[33] However, the addition of a single element may not always be adequate to achieve significant improvements in performance. Co-doping of g-C_3N_4 with various elements can further accelerate the rate of electron–hole pair separation. For instance, the co-doping of S and Cl in g-C_3N_4 results in an augmentation of the specific surface area, modulation of the band gap, and facilitation of charge migration as well as an upward shift in the conduction band.[34]

Herein, a novel feathery P and S co-doped CN catalyst featuring an expanded network of pores $P_{0.3}S_{0.2}$-CN was successfully synthesized by hydrothermal procedure (Fig. 1). The incorporation of P and S elements not only enhances the efficiency of carrier separation, but also significantly boosts its redox ability compared to single doping. Experimental results illustrate that the active species $^{\bullet}O_2^-$ plays a major role in driving the photocatalytic process. Under visible light irradiation, the photocatalytic H_2O_2 production rate of $P_{0.3}S_{0.2}$-CN reaches 28.6 mg L^{-1} h^{-1} and it degrades TC with a removal efficiency of 87.3%. Compared to the photocatalysts $P_{0.5}$-CN and $S_{0.4}$-CN, the H_2O_2 yield rate of $P_{0.3}S_{0.2}$-CN exhibited increases of 28.67% and 53.28%, respectively, and TC degradation rate increases of 15.2% and 11.5%, respectively. Moreover, we conducted a comprehensive analysis of differential charge and Bader charges to elucidate the exceptional co-doping

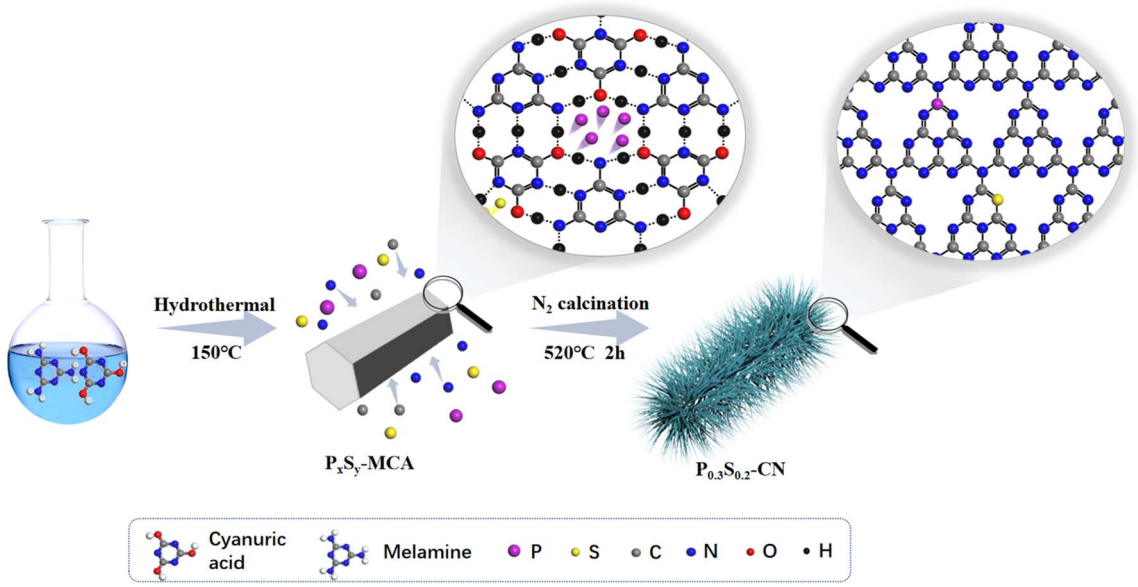

Fig. 1 Schematic depiction of the fabrication process of P_xS_y-CN.

performance through DFT calculations. The experimental and computational evidence both support $P_{0.3}S_{0.2}$-CN as an efficient catalytic material for synthetic H_2O_2 and TC degradation.

2. Experimental section

All reagents employed in this work were of analytical or chromatographic grade. The experiments were conducted using ultra-pure water with a conductivity of less than 0.2 μs cm^{-1}. The pH adjustment was performed utilizing diluted aqueous solutions of NaOH and H_2SO_4. The synthesis process of doped carbon nitride and the subsequent photocatalytic performance testing are provided in the ESI.†

3. Results and discussion

The information regarding the crystalline structure and phase composition of carbon nitride is presented in Fig. 2a. Two additional distinctive characteristic peaks are observed at approximately 13° and 27° in the XRD diffractograms, corresponding to the (100) and (002) crystallographic planes of carbon nitride, respectively. This observation suggests that the morphology control and doping have not altered its crystal structure. Interestingly, the diffraction peaks of the doped CN are shifted due to the difference in electronegativity between the different atoms. Doping reduces the attraction between the carbon and nitrogen layers, thereby increasing the spacing and ultimately causing a downward shift in the diffraction peaks.[33] The broad absorption peaks observed in Fig. 2b, ranging from 3100 to 3600 cm^{-1}, can be attributed to the stretching vibrations of $-NH_2$, –NH and –OH groups. These peaks may arise from the residual amine groups and surface H_2O molecules resulting from the incomplete condensation of the precursors.[31] The absorption peak at 818 cm^{-1} is assigned to the bending vibration of the tri-*s*-triazine unit. No co-doping of P and S was observed, as these peaks overlapped with the C–N vibration peaks.[35] The spectrum of $P_{0.3}S_{0.2}$-CN exhibits an additional peak at 534 cm^{-1}, which can potentially be attributed to the P–S stretching mode.[36] The N_2 adsorption–desorption isotherms of the CN and $P_{0.3}S_{0.2}$-CN samples are depicted in Fig. S1a and b.† Both CN and $P_{0.3}S_{0.2}$-CN catalysts adhere to the IUPAC classification criteria for type IV adsorption isotherms, indicating the presence of mesoporous structures in the sample. The specific surface areas of CN and $P_{0.3}S_{0.2}$-CN are 33.45 and 48.23 $m^2\ g^{-1}$, respectively, with corresponding pore sizes of 24.74 and 20.43 nm. The specific surface area of $P_{0.3}S_{0.2}$-CN is 5.84 times greater than that of the g-C_3N_4 prepared in the literature (8.25 $m^2\ g^{-1}$).[34] $P_{0.3}S_{0.2}$-CN exhibits a higher specific surface area and superior porosity, thus offering an increased number of reactive sites for photocatalytic reactions and facilitating adsorption of organic pollutants.[37]

The chemical composition and atomic state information of the samples were analyzed using X-ray photoelectron spectroscopy (XPS). Fig. S2† displays the complete spectra of CN and $P_{0.3}S_{0.2}$-CN, revealing the presence of the elements C, N, and O. High resolution XPS was employed to further elucidate the chemical state of each element in the samples. The binding energy of C 1s, as shown in Fig. 2c, is deconvoluted into three distinct peaks at 284.8 eV, 288.2 eV and 293.5 eV corresponding to the C–C bond, C–N=C bond and π excitation bond of CN,

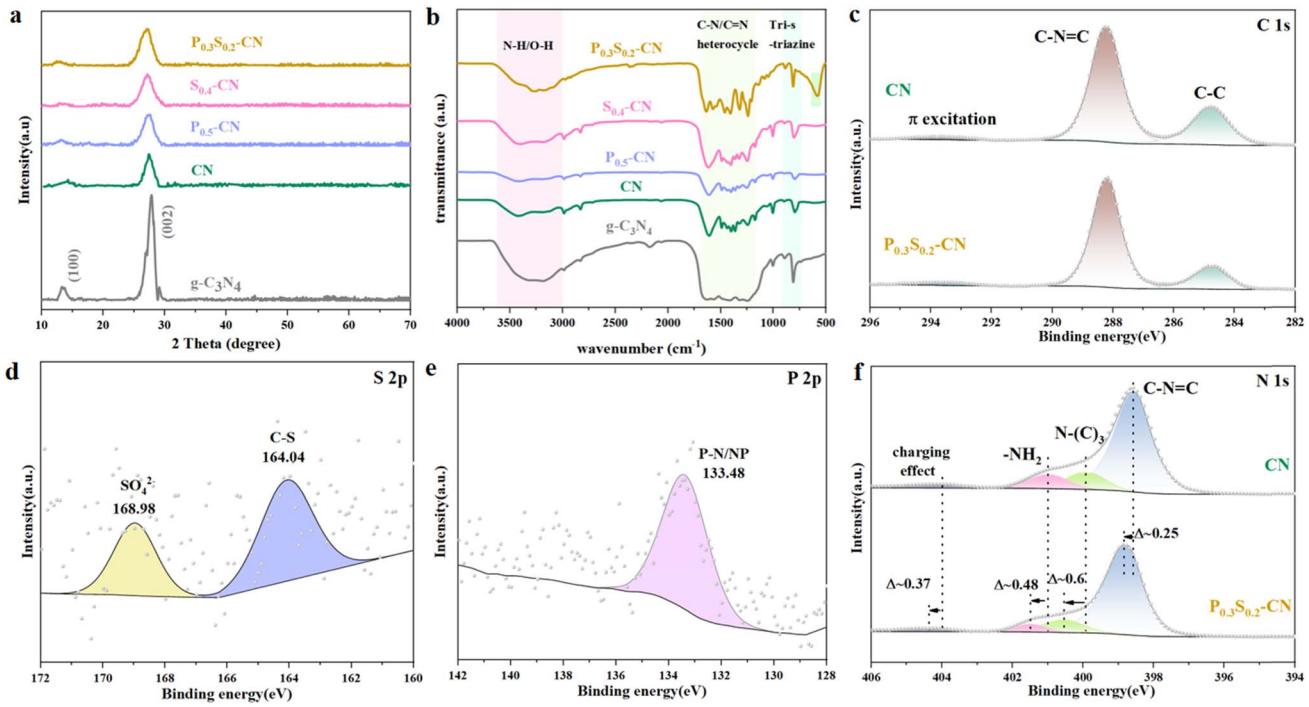

Fig. 2 (a) XRD diffraction patterns, (b) FT-IR spectra, and XPS (c) C 1s spectra, (d) S 2p spectra, (e) P 2p spectra, and (f) N 1s spectra of various samples.

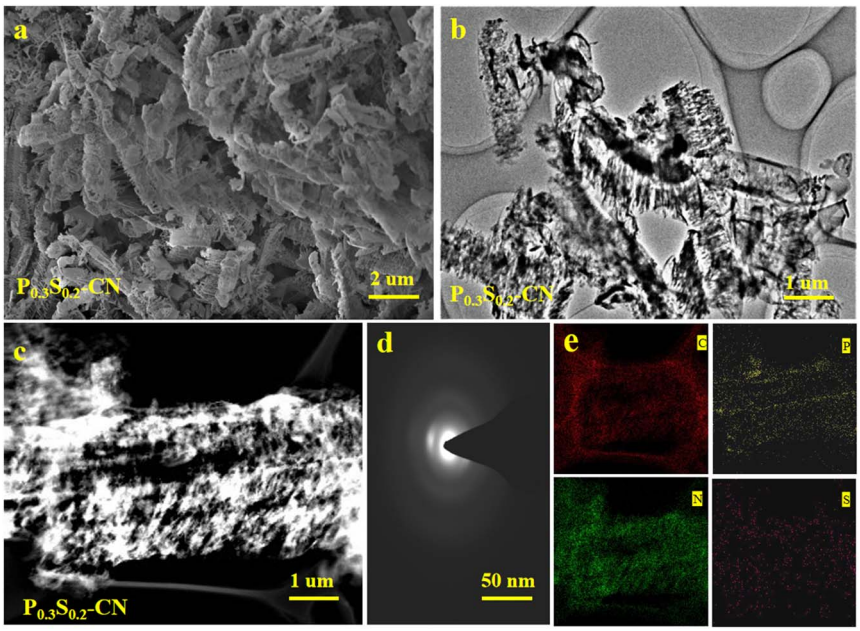

Fig. 3 (a) SEM, (b) and (c) TEM, (d) selected area electron diffraction and (e) EDS mapping images of $P_{0.3}S_{0.2}$-CN.

respectively. Four discernible peaks are observed in the N 1s spectrum of CN: the C–N=C bond (398.17 eV), N–$(C)_3$ bond (399.93 eV), amino functional group (400.90 eV) and charging effect (403.75 eV).[38,39] The binding energies of the four peaks of in the N 1s spectrum of $P_{0.3}S_{0.2}$-CN are shifted to varying degrees towards higher binding energies. This shift is due to the formation of new coordination bonds between N and P atoms which lead to the extra electron redistribution because of the nonmetal-doping. Simultaneously, the electron density around the N atoms decreases, leading to a shift of the four N 1s peaks in $P_{0.3}S_{0.2}$-CN to higher binding energies.[40] The S 2p spectrum primarily shows binding energies at 164.04 eV and 168.98 eV, corresponding to the C–S bond[41] within the nitrogen aromatic ring and the sulfur oxides released during thermal polymerization, respectively. The presence of a prominent peak at 133.48 eV in the P 2p spectrum, attributed to P–N coordination, signifies the substitution of C with P in the heptazine ring.[42] Based on the aforementioned XPS analysis, successful replacement of C and N atoms by P and S atoms respectively occurred in the carbon nitride.

The morphology and surface characteristics of the obtained samples are examined using scanning electron microscopy (SEM) and transmission electron microscopy (TEM), respectively. As depicted in Fig. S3,† the introduction of ammonium dihydrogen phosphate did not alter the rod-like morphology of MCA, thereby providing a certain acidic environment conductive to promoting the hydrolysis of MA into partial CA and serving as a source for phosphorus-doped carbon nitride. Conversely, when thiourea was added to the MCA supramolecule, it induced a flat and uniform orientation, resulting in the transformation of MCA rods into a planar stick-like shape.[43] The stable hydrogen bond structure in MCA allows the vertical outflow of NH_3 and other gases during calcination, resulting in the formation of a specific hollow CN structure. Fig. S4a and b† demonstrates that, as the phosphate content increases, P_x-CN undergoes a transformation from fragmented hollow tubes to flat tubes.[44] The morphology of S_y-CN undergoes changes at elevated temperatures (Fig. S4c†). With incorporation of thiourea, the morphology continuously changes as NH_3 and other gases are released from the interior to the exterior during calcination. The diverse modes of phosphate binding, along with thiourea and MA-CA, lead to apparent alterations in the morphology of the final $P_{0.3}S_{0.2}$-CN. As shown in Fig. 3a–c, $P_{0.3}S_{0.2}$-CN exhibits a planar feather-like structure and a 2D irregular planar structure with an enlarged pore network. The selected area electron diffraction (SAED) image in Fig. 3d reveals that the diffraction rings are unclear and have blurred edges, indicating the poor crystallinity of the $P_{0.3}S_{0.2}$-CN.[45–47] Elemental mapping (Fig. 3e) confirms the presence of the elements C, N, S, and P in $P_{0.3}S_{0.2}$-CN. However, it is noted that under high-temperature conditions, elemental S tends to volatilize with the gas, resulting in a reduced content.

The UV-vis DRS are presented in Fig. S5.† For g-C_3N_4, it exhibits significant absorption within the range of 200–450 nm with an absorption edge value of approximately 450 nm. In contrast, the light absorption of $P_{0.3}S_{0.2}$-CN is significantly enhanced by the co-doping of P and S elements, resulting in an extended edge range from 450 to 750 nm. The introduction of P and S elements along with the unique morphological structure accelerates the light trapping ability, leading to the generation of photo-induced carriers. As depicted in Fig. 4a, the band gap energy for $P_{0.3}S_{0.2}$-CN was calculated to be 2.45 eV. The VB position ratio of CN to the normal hydrogen electrode was determined at pH = 7.[48] The CB positions were obtained through combined band gap and $E_{VB\text{-}XPS}$ analysis. Notably, $P_{0.3}S_{0.2}$-CN possesses the highest negative CB position (ranging

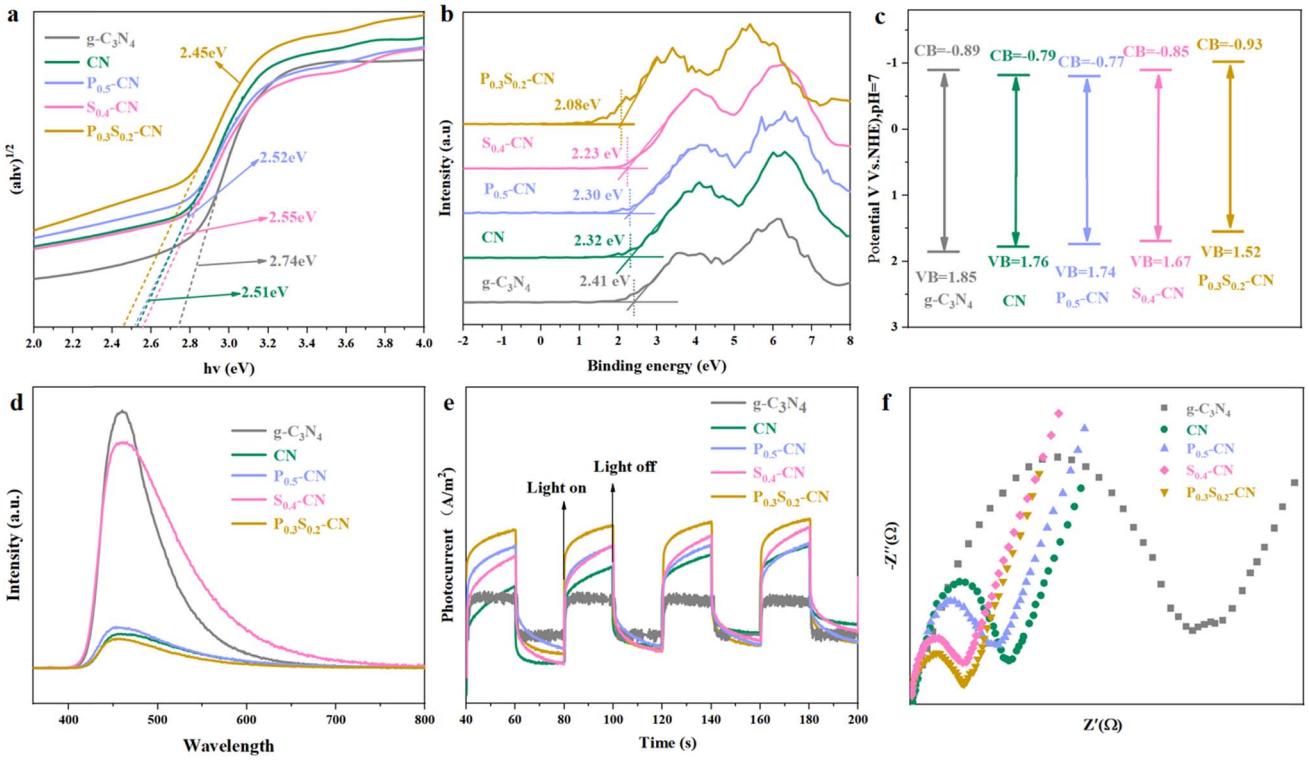

Fig. 4 (a) Band gap values, (b) VB-XPS, (c) energy band structure, (d) PL spectra, (e) TPC spectrograms, (f) EIS plots of various species.

from 1.52 to 0.93) and the narrowest band gap, as shown in Fig. 4b and c, indicating that electrons can be more easily excited into the CB and promoting a stronger reduction reaction involving photo-generated e^- and h^+. The extent of complexation between photo-generated e^- and h^+ can be evaluated by PL spectroscopy. The PL emission spectra were excited under a wavelength of 360 nm, and the peaks were centered at around 457 nm. As depicted in Fig. 7, $P_{0.3}S_{0.2}$-CN shows the lowest PL peak intensity which indicates that neither P nor S acts as a recombination center for photo-generated electrons and holes in CN. Fewer electrons are recombining with holes and leaving the conduction band, resulting in lower photon energy. This suggests that the recombination rate of electrons and holes is suppressed, meaning the separation efficiency of the electron–hole pairs is higher.[49,50] The blue shift observed in doped CN's PL spectrum may be attributed to changes in its band gap caused by doping.[51] TPC curves are displayed in Fig. 4e; remarkably, the photocurrent response of $P_{0.3}S_{0.2}$-CN is superior to those of the other samples which suggests a prolonged lifetime for photo-generated carriers. Furthermore, the Nyquist diagram reveals that the arc radius for $P_{0.3}S_{0.2}$-CN photocatalyst is smaller than those of the others (Fig. 4f), suggesting that doping with both P and S elements reduces charge transfer resistance, thereby facilitating rapid separation and transfer of photoinduced charges.

The photocatalytic H_2O_2 generation performance of various carbon nitrides under visible light irradiation was investigated under natural pH conditions. As shown in Fig. 5a, the H_2O_2 yield of hydrothermal-calcined CN is 3.8 times higher than that of directly calcined g-C_3N_4, which can be attributed to the formation of a partially tubular structure and hydrophilic functional groups on the surface of CN.[52] By adjusting the ratio of ammonium dihydrogen phosphate ($NH_4H_2PO_4$), the optimum $P_{0.5}$-CN was found to produce H_2O_2 at a concentration of 1.308 mM (Fig. S6a†). Varying the amount of thiourea resulted in $S_{0.4}$-CN producing H_2O_2 at a concentration of 1.098 mM (Fig. S6b†). These results indicate that the appropriate amounts of P and S doping could significantly enhance the production performance of photocatalytic H_2O_2. As depicted in Fig. S6c,† four P_xS_y-CN photocatalysts with different P and S contents were prepared by varying the amounts of $NH_4H_2PO_4$ and thiourea, all exhibiting higher H_2O_2 generation performance compared to the mono-doped P or S CN catalysts. After 120 min of photocatalytic reaction, $P_{0.3}S_{0.2}$-CN accumulated an H_2O_2 concentration as high as 1.683 mM under visible light irradiation, surpassing the other catalysts' performance in terms of H_2O_2 generation. The above findings indicate that co-doping plays a facilitating role and the appropriate amounts of P and S doping can significantly improve the photocatalytic production of H_2O_2. The yield of H_2O_2 produced by $P_{0.3}S_{0.2}$-CN is 28.6 mg L^{-1} h^{-1}, which exceeds the yield reported in previous literature (Table S1†).

Decomposition experiments were conducted to investigate the proportion of $P_{0.3}S_{0.2}$-CN that decomposes H_2O_2 during the photocatalytic reaction. As shown in Fig. S6e,† a slight reduction in H_2O_2 concentration (0.591 mM) was observed after 120 min of light exposure. The control experiment without $P_{0.3}S_{0.2}$-CN demonstrated H_2O_2 production at a concentration of

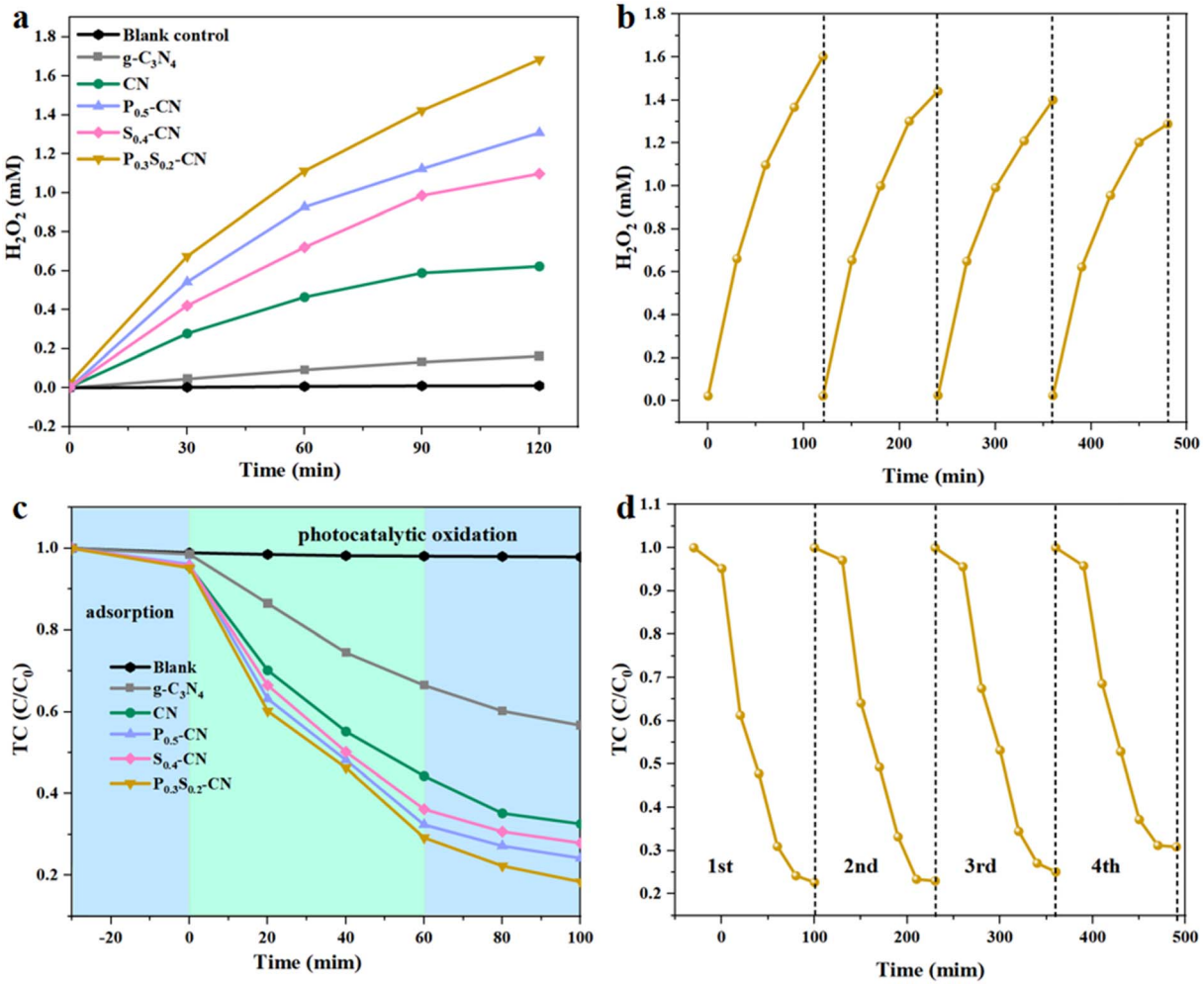

Fig. 5 (a) Photocatalytic production of H_2O_2 by various photocatalysts, (b) 50 mg photocatalyst for 4 consecutive cycles of H_2O_2 production, (c) photocatalytic oxidative degradation of TC (20 mg L^{-1}) by multifarious catalysts (30 mg), and (d) 30 mg photocatalyst employed for 4 consecutive cycles of TC degradation.

0.011 mM (Fig. S6f†), yielding an H_2O_2 decomposition efficiency of 3.33%.

TC was selected as a representative pollutant to evaluate the photocatalytic properties of the various carbon nitrides under visible light. All photocatalytic reactions were carried out until adsorption–desorption equilibrium was reached under dark stirring conditions. As shown in Fig. 5c, the TC concentration remained essentially unchanged in the absence of light. With the exception of g-C_3N_4, the other CN photocatalysts exhibited higher adsorption capacity for TC, which can be attributed to their relatively larger specific surface area. For the photocatalytic degradation experiments with 30 mg photocatalysts and an initial TC concentration of 20 mg L^{-1}, $P_{0.3}S_{0.2}$-CN, $P_{0.5}$-CN, $S_{0.4}$-CN, CN, and g-C_3N_4 achieved degradation capacities of 80.6%, 72.1%, 75.8%, 67.4%, and 43.3%, respectively (Fig. S7a†), with pseudo primary kinetic rate constants of 0.0163 min^{-1}, 0.0126 min^{-1}, 0.0140 min^{-1}, 0.0110 min^{-1}, and 0.00567 min^{-1}, respectively (Fig. S7a†). The kinetics analysis revealed that $P_{0.3}S_{0.2}$-CN exhibited superior photocatalytic degradation efficiency compared to the other carbon nitride materials due to its co-doping effect and presence of more reactive sites. After each experiment, the photocatalysts were washed with deionized water and vacuum dried for subsequent use. The recycling test showed a gradual decrease in both TC removal rate and H_2O_2 yield compared to their initial values (Fig. 5b and d). The slight decrease in photocatalytic performance may be ascribed to the loss of some active sites caused by adsorption from reaction products. We conducted Fourier transform infrared spectroscopy (Fig. S7e†) testing on the $P_{0.3}S_{0.2}$ photocatalyst after four cycles of photocatalytic activity. The characteristic peaks of the original functional groups remained unchanged, indicating that the photocatalyst exhibits good stability.

According to Fig. 6a, the introduction of Fe^{2+} before the reaction resulted in a higher photocatalytic degradation efficiency of $P_{0.3}S_{0.2}$-CN compared to $P_{0.3}S_{0.2}$-CN without treatment after 60 min of photocatalytic oxidation. However, adding Fe^{2+} before light did not enhance the degradation performance. Thus, the combination of photocatalytic oxidation and Fenton oxidation (two-step oxidation) accelerated the photocatalytic

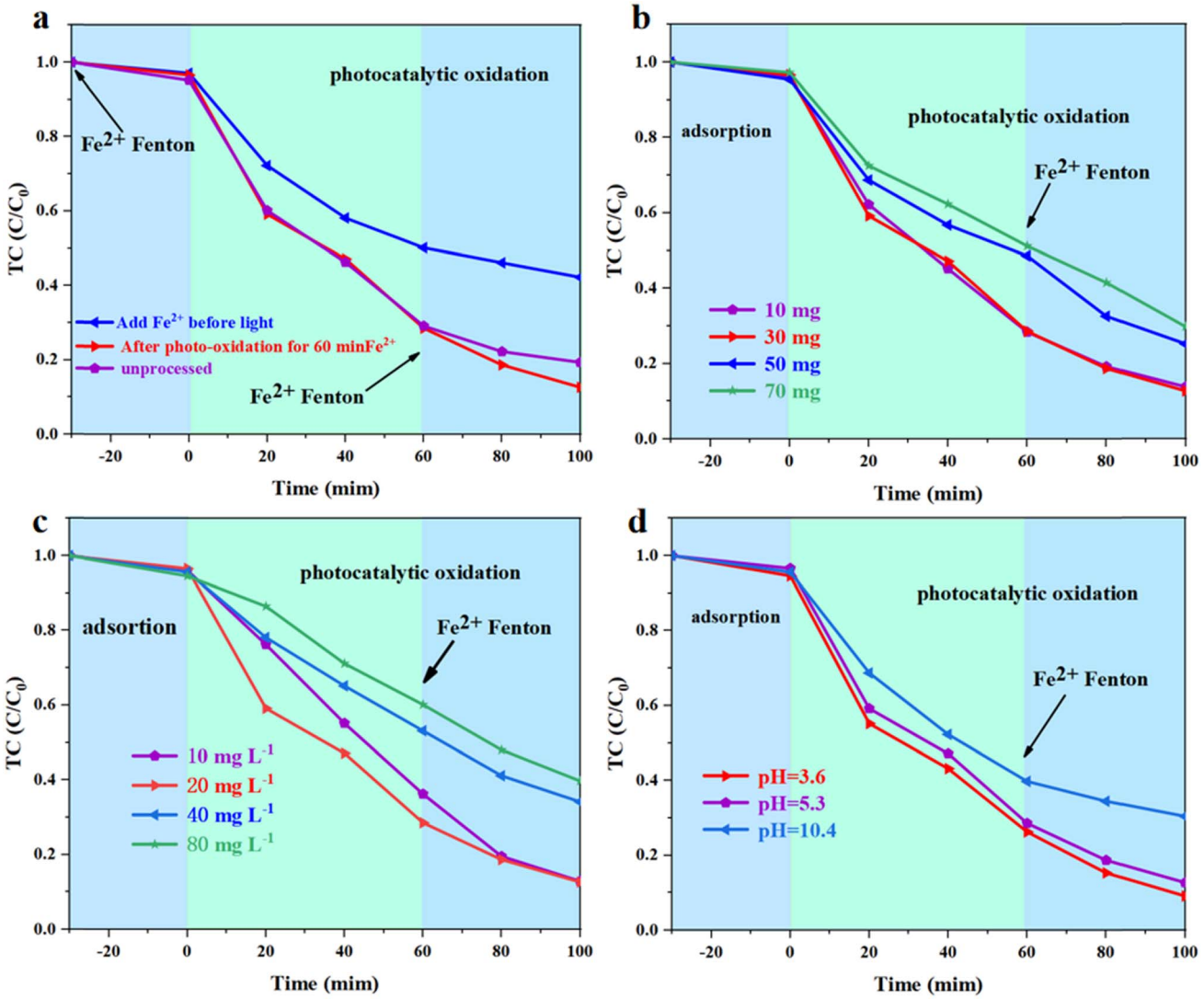

Fig. 6 Under visible light irradiation, effect of (a) Fe^{2+} addition on the photocatalytic degradation of TC by $P_{0.3}S_{0.2}$-CN, (b) dosage of the $P_{0.3}S_{0.2}$-CN catalyst, (c) initial concentration of TC, (d) different pH values on photocatalytic oxidation-Fenton oxidative degradation.

degradation process. The effect of $P_{0.3}S_{0.2}$-CN dosage (10–70 mg) on TC removal efficiency was investigated under visible light photocatalytic oxidation-Fenton oxidation (Fig. 6b and S7b†). It was found that when an excessive amount of carbon nitride catalyst was utilized, there was a marked decrease in photoactivation volume due to the increase solution turbidity.[53] Fig. 6c and S7c† display the effect of different initial TC concentrations on $P_{0.3}S_{0.2}$-CN catalyzed TC degradation efficiency and its corresponding pseudo primary reaction kinetics. The final photodegradation efficiency remained essentially unchanged when increasing TC concentration from 10 mg L^{-1} to 20 mg L^{-1}. Nevertheless, when TC concentration was further increased from 20 mg L^{-1} to 80 mg L^{-1}, there was an apparent suppression in photocatalytic degradation efficiency with a corresponding decrease in kinetic constant k_{pfo} from 0.0201 min^{-1} to 0.0089 min^{-1}. The decrease in the photodegradation efficiency can be attributed to both high TC concentration and limited activity of intermediate products competing for active sites on the photocatalyst. As shown in Fig. 6d and S7d,† reducing the initial pH from 5.3 to 3.6 led to an increase in reaction rate constant from 0.0201 min^{-1} to 0.0229 min^{-1}, implying the excellent performance of the photocatalytic oxidation-Fenton oxidation system under acidic conditions. However, adjusting the pH to 10.7 brought about a notable decrease in the reaction rate constant (0.0115 min^{-1}). The observations suggest that $P_{0.3}S_{0.2}$-CN has the ability to generate a greater amount of reactive substances in acidic conditions.

To investigate the effect of P and S doping on catalytic activity, we performed DFT analog calculations on the CN and $P_{0.3}S_{0.2}$-CN. Fig. S8† illustrates the optimized structures of the top and side of the CN, P–CN, S–CN, and $P_{0.3}S_{0.2}$-CN catalytic surfaces. Fig. S9† presents the theoretical calculated band structures for CN and $P_{0.3}S_{0.2}$-CN. It is observed that the bandgap value decreases significantly after doping CN with P and S elements, and a smaller bandgap is more favorable for

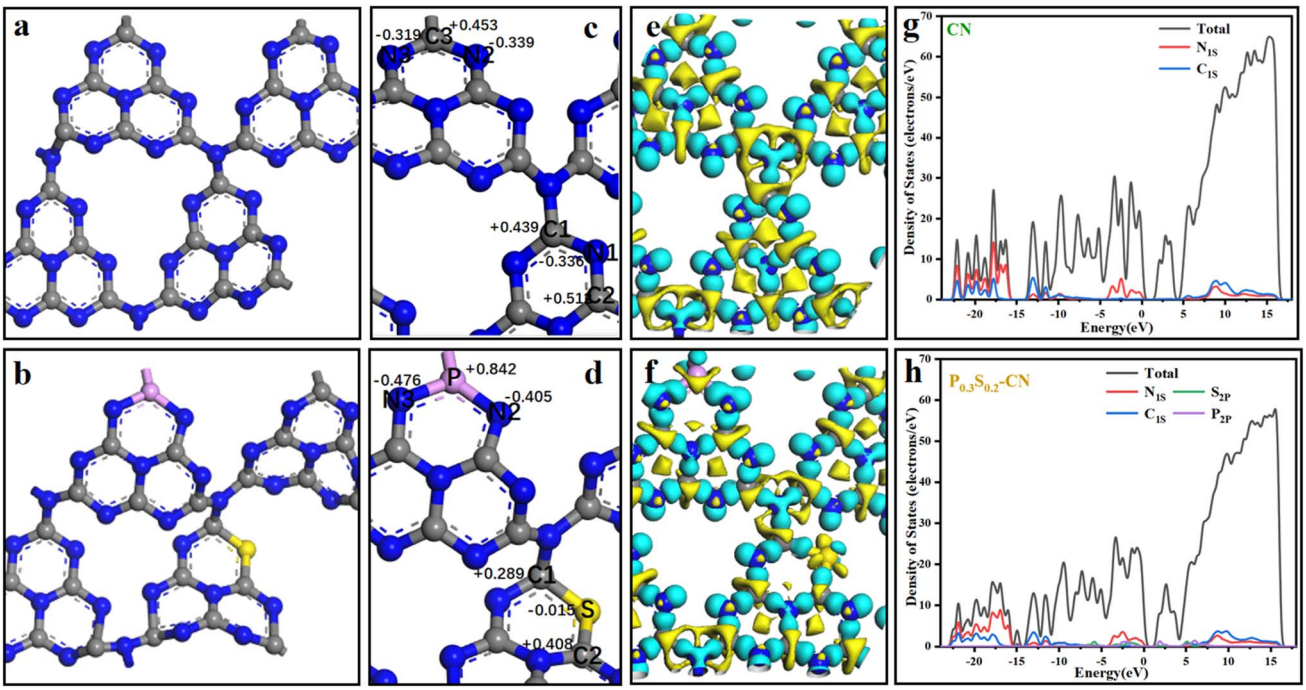

Fig. 7 The optimized structures of the (a) CN and (b) $P_{0.3}S_{0.2}$-CN; the DFT-computed atomic charges at the (c) CN and (d) $P_{0.3}S_{0.2}$-CN doping sites are provided near each atom. The differential charge density plots of (e) CN and (f) $P_{0.3}S_{0.2}$-CN. DOS plots of (g) CN and (h) $P_{0.3}S_{0.2}$-CN.

electron migration, improving the photoelectrochemical performance of the material. However, the calculated bandgap values for semiconductors are often greatly underestimated; therefore, relying solely on theoretically calculated bandgap values to analyze trends is not recommended.[54] We computed the atomic charges near the doping sites of CN and $P_{0.3}S_{0.2}$-CN to gain further insights. The optimized top surface structures of CN and $P_{0.3}S_{0.2}$-CN catalytic surfaces are presented in Fig. 7a and b, respectively. As shown in Fig. 7d, the atomic charge of the C-bound S atom is −0.015 eV, while that of the N-bound P atom exhibits a larger positive value. Specifically, within the P–N bond, we observed atomic charges for the P, N2, and N3 atoms of +0.842, −0.405, and −0.476, respectively. Our findings display that doping leads to a reduction in the charges of the C1

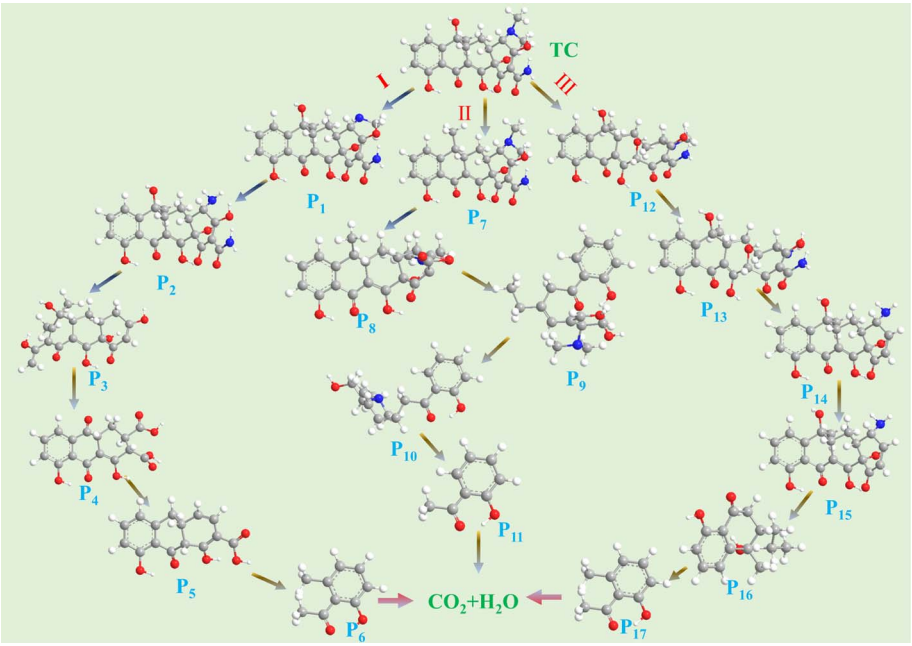

Fig. 8 Photocatalytic degradation pathway of TC in aqueous solution by $P_{0.3}S_{0.2}$-CN under visible light irradiation.

and C2 atoms in CN, while S exhibits higher positivity compared to N1. The charges of the N2 and N3 atoms in CN decrease, with the P atoms carrying larger positive charges. Notably, the positive charge of P surpasses that of C3, indicating the replacement of N1 by S and C3 by P through covalent bonding with neighboring N. This formation of a conjugated system exhibits a more pronounced conjugation effect than an induced effect, resulting in a high electrostatic potential surface conducive to adsorption and activation of the adsorbent. The differential charge densities on the surfaces of CN and $P_{0.3}S_{0.2}$-CN are depicted in Fig. 7e and f, respectively. Upon S substitution doping, the original N1 of CN undergoes a transition from electron acquisition to electron loss, while the corresponding C3 becomes more prominent in its original state of electron loss after P doping. The DOS of CN and $P_{0.3}S_{0.2}$-CN surfaces were calculated and are shown in Fig. 7g and h, respectively. We found that after doping CN with P and S elements, the P 2p and S 2p orbital energy levels appear near the Fermi level. In $P_{0.3}S_{0.2}$-CN, the conduction band edge moves closer to the Fermi level, resulting in a reduced bandgap. A smaller bandgap allows electrons to more easily transition from the valence band to the conduction band, thereby enhancing the material's photoelectrochemical performance.

Importantly, the potential photodegradation pathways and intermediates of TC proposed by LC-MS are shown in Fig. 8. Mass spectrometry inferred seventeen possible intermediates involved in the oxidation process of TC, and their molecular and structural formulas are present in Table S3.† In pathway I, two demethylations yield intermediate P_2 (m/z = 416), while deamidation reactions lead to the formation of intermediate P_3 (m/z = 358). The C=C bond breaking generates intermediate product P_4 (m/z = 322). Notably, P6 can be oxidized by the resulting $^{\bullet}O_2^-$ to form small molecule P_7 (m/z = 150) through a series of C–C bonding, C=C bond breaking and ring opening reactions.[55] Pathway II involves conversion to P_8 (m/z = 411) *via* dehydroxylation and cyclo-decomposition followed by C–C bond breakage and sequential oxidation resulting in P_{11} (m/z = 136). In pathway III, C–C bond breaking and demethylation

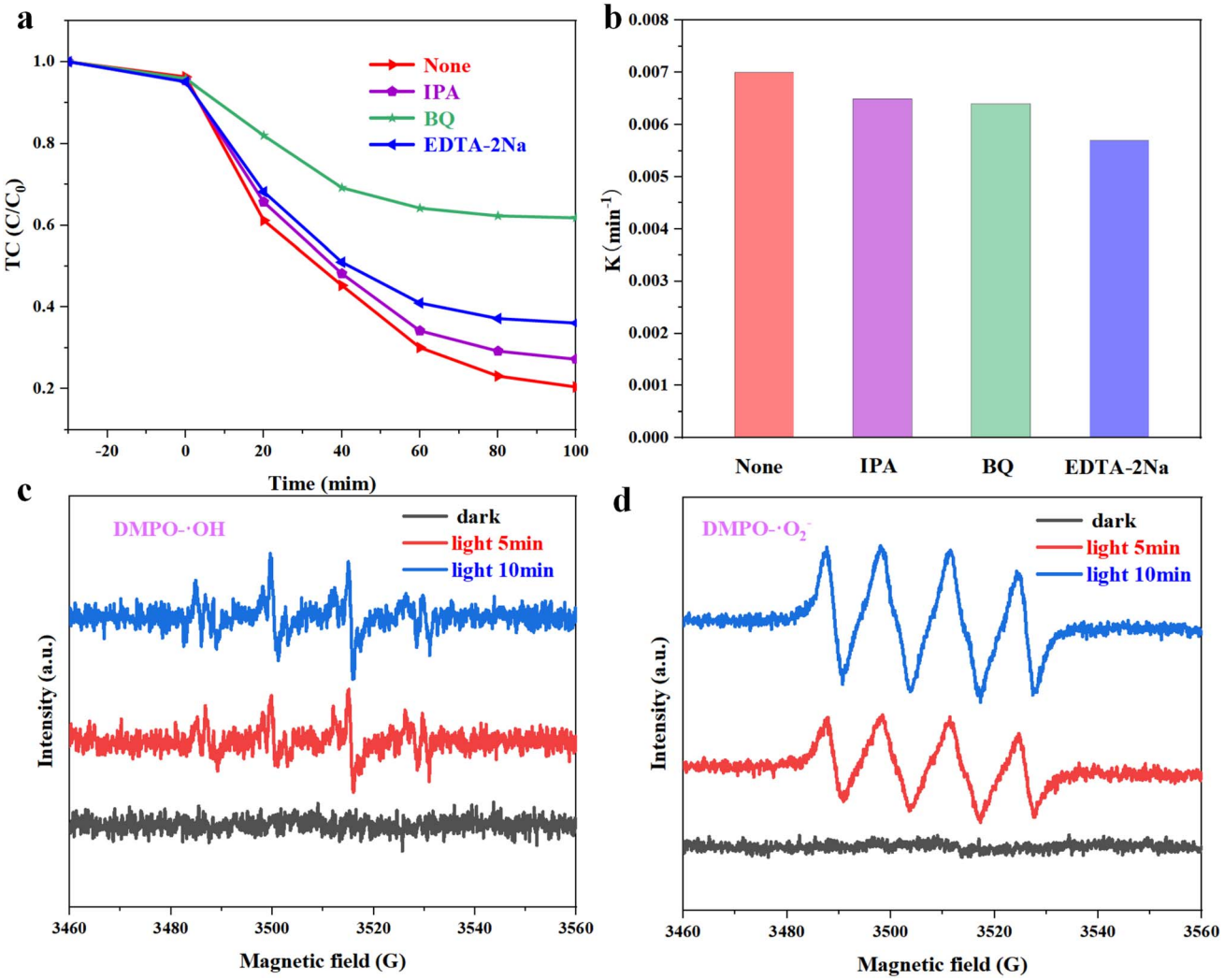

Fig. 9 Under visible light irradiation and added scavenger conditions, (a) TC and (b) corresponding kinetic constants of $P_{0.3}S_{0.2}$-CN degradation and EPR spectra of $P_{0.3}S_{0.2}$-CN in the dark and under visible light irradiation with (c) DMPO-$^{\bullet}$OH and (d) DMPO-$^{\bullet}O_2^-$.

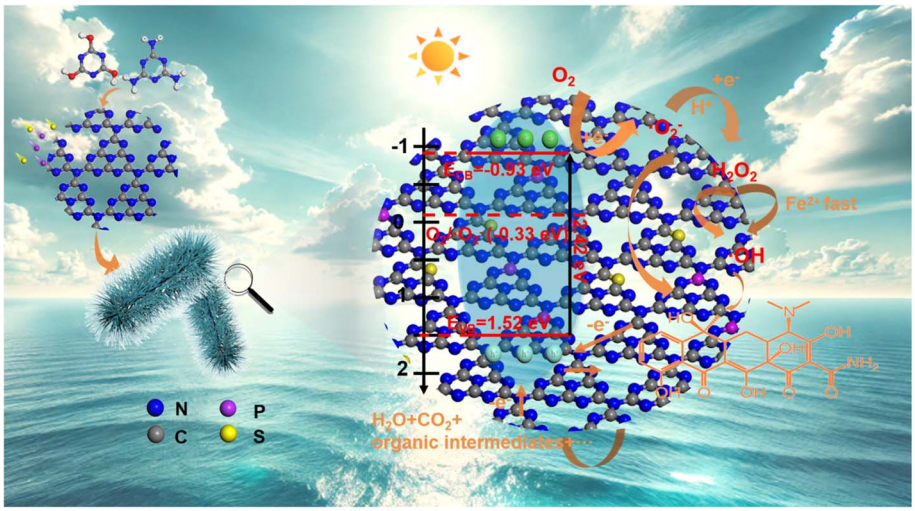

Fig. 10 Mechanism diagram of the photocatalytic two-step oxidation by $P_{0.3}S_{0.2}$-CN.

produce intermediate P_{13} (m/z = 418), while atomic rearrangement allows for dehydroxylation and deamidation leading to the formation of P_{14} (m/z = 357). Oxidation of double bonds within TC triggers ring opening reactions yielding P_{15} (m/z = 331), after which radical decomposition oxidizes C=C bonds, amide groups, $-CH_3$ groups, and $-N(CH_3)_2$ groups, forming smaller molecules. Finally, these intermediates undergo further oxidation, causing compounds such as CO_2, H_2O, and so on.

The main active species of responsible for TC degradation in $P_{0.3}S_{0.2}$-CN were investigated by radical trapping experiments, as depicted in Fig. 9a. Isopropyl alcohol (IPA), *p*-benzoquinone (BQ), and EDTA-2Na were employed as scavengers of hydroxyl radicals ($^{\bullet}OH$), superoxide radicals ($^{\bullet}O_2^-$), and h^+. The addition of IPA and EDTA-2Na brought about a decrease in the removal rate of TC from 79.4% to 72.8% and 63.9%, respectively, suggesting that the impact of $^{\bullet}OH$ and h^+ on the degradation efficiency was limited. However, when BQ was introduced, the removal rate of TC dropped to only 38.2%, with a corresponding decrease in kinetic rate from 0.007 min^{-1} to 0.0034 min^{-1} (Fig. 9b). This indicates that $^{\bullet}O_2^-$ played a crucial role in the TC degradation process. To further validate the generation of $^{\bullet}O_2^-$ and $^{\bullet}OH$ in $P_{0.3}S_{0.2}$-CN, electron spin resonance (ESR) spectroscopy employing DMPO (5,5-dimethyl-1-pyrroline-N oxide) as a spin trap was utilized. As shown in Fig. 9c and d, under dark conditions, the intensity of DMPO-$^{\bullet}OH$ and DMPO-$^{\bullet}O_2^-$ was negligible. However, under light irradiation, DMPO-$^{\bullet}OH$ (intensity ratio of 1 : 2 : 2 : 1) and DMPO-$^{\bullet}O_2^-$ (intensity ratio of 1 : 1 : 1 : 1) exhibited increased intensity with prolonged irradiation time.[56,57] The results indicate that $P_{0.3}S_{0.2}$-CN can continuously generate $^{\bullet}OH$ and $^{\bullet}O_2^-$ under visible light irradiation. In the photocatalytic system involving $P_{0.3}S_{0.2}$-CN, O_2 can be reduced *via* two-electron transfer to produce $^{\bullet}O_2^-$, some portion of which is further reduced to H_2O_2, while another part of $^{\bullet}O_2^-$ plays a dominant role in the photocatalytic degradation. Furthermore, the involvement of $^{\bullet}OH$ is observed during this degradation process.

Based on the aforementioned results, a proposed mechanism diagram of $P_{0.3}S_{0.2}$-CN during the photocatalytic two-step oxidation is shown in Fig. 10. Upon visible light irradiation, photo-generated electrons migrate from the VB to the CB, while h^+ is produced on the VB.[58,59] Because of the more negative potential of $P_{0.3}S_{0.2}$-CN (−0.93 eV) compared to $O_2/^{\bullet}O_2^-$ (−0.33 eV), the photoinduced e^- reduces O_2 to $^{\bullet}O_2^-$ on the CB. A portion of $^{\bullet}O_2^-$ can directly oxidize TC, leading to the formation of some organic intermediates,[60] while others can be reduced to H_2O_2. Since the energy level of h^+ in the photocatalyst VB (1.52 eV) is lower than $E(^{\bullet}OH/H_2O = 2.68$ eV *vs.* NHE), it suggests that h^+ lacks sufficient energy for oxidizing H_2O and producing $^{\bullet}OH$.[61,62] Nevertheless, h^+ can capture photogenerated e^- and use them for oxidizing TC as well as its organic intermediates. During photocatalytic degradation, H_2O_2 activates e^- to generate $^{\bullet}OH$, which further accelerates the TC degradation process through the Fenton reaction. Eventually, TC is degraded into small molecules and harmless substances such as CO_2 and H_2O.[63]

4. Conclusions

In this study, we successfully synthesized a feathery multifunctional $P_{0.3}S_{0.2}$-CN photocatalyst with an enlarged pore network using a hydrothermal technique. Demonstrating a notable photocatalytic H_2O_2 production rate of 28.6 mg L^{-1} h^{-1} under visible light, $P_{0.3}S_{0.2}$-CN also achieves an impressive 87.3% efficiency in degrading TC. When compared to the singly doped photocatalysts $P_{0.5}$-CN and $S_{0.4}$-CN, $P_{0.3}S_{0.2}$-CN shows a significant enhancement in H_2O_2 yield by 28.67% and 53.28%, respectively, and TC degradation by 15.2% and 11.5%. The catalyst's exceptional performance is attributed to the synergistic effects of phosphorus and sulfur co-doping, which not only enhances charge carrier separation but also improves the redox capabilities more effectively than single-doping strategies. Density functional theory calculations reveal that co-doping leads to electron clustering near heteroatoms and

enhances carrier migration and separation on the catalytic surface of graphitic carbon nitride. This research provides a pioneering approach in designing high-efficiency catalysts for the degradation of organic pollutants, showcasing significant advancements in photocatalyst development by optimizing elemental doping strategies to enhance photocatalytic activity.

Data availability

The data supporting this article have been included as part of the ESI.†

Author contributions

Lian Qin: writing –review & editing, conceptualization, supervision, methodology; Zhongli Zhao: Project conceptualization, experimentation, formal analysis, modify; Ning Fu: material synthesis and characterization, supervision, data arrangement; Xiangyu Li: investigation, formal analysis; Lei Hu: software, laboratory aids, methodology, formal analysis. Xingang Li: conceptualization, investigation; Chun Zhang: writing – review & editing, resources funding.

Conflicts of interest

There are no conflicts to declare.

Acknowledgements

We acknowledge the financial support of the Key Research and Development Plan of Gansu Province (No. 22YF7GA148).

References

1 Z. Wei, J. Liu and W. Shangguan, *Chin. J. Catal.*, 2020, **41**, 1440–1450.
2 P. Tenorio-Chávez, G. A. Elizalde-Velázquez, L. M. Gómez-Oliván and M. D. Hernández-Navarro, *Sci. Total Environ.*, 2023, **859**, 159731.
3 Y. Lee, D. L. Sedlak and U. von Gunten, *Environ. Sci. Technol.*, 2023, **57**, 18391–18392.
4 Q. Zou, B. Wang, B. Gao, T. Jiang, Q. Feng, M. Chen, J. Zhang and X. Zhang, *Biochar*, 2023, **5**, 1–24.
5 J. Zhang, G. Zhang, Q. Ji, H. Lan, J. Qu and H. Liu, *Appl. Catal., B*, 2020, **266**, 118665.
6 J. Xu, Q. Zhang, X. Gao, P. Wang, H. Che, C. Tang and Y. Ao, *Angew. Chem., Int. Ed.*, 2023, **62**, e202307018.
7 X. Yang, X. Zeng, H. Chen, L. Xin, J. Pan, H. Ji and K. Cheng, *Chem. Eng. J.*, 2024, **483**, 148697.
8 X. Zhang, J. Tang, L. Wang, C. Wang, L. Chen, X. Chen, J. Qian and B. Pan, *Nat. Commun.*, 2024, **15**, 917.
9 M. Wu, X. Guo, Y. Cao, H. Yu, Z. Hu, Y. Yang, T. Yao and J. Wu, *Chem. Eng. J.*, 2024, **489**, 151091.
10 A. Torres-Pinto, H. Boumeriame, C. G. Silva, J. L. Faria and A. M. T. Silva, *ACS Sustainable Chem. Eng.*, 2023, **11**, 894–909.
11 L. Xie, T. Zhang, X. Wang, W. Zhu, Z. Liu, M. Liu, J. Wang, L. Zhang, T. Du, C. Yang, M. Zhu and J. Wang, *J. Cleaner Prod.*, 2022, **359**, 131808.
12 M. Yang, W. Wang, H. Ma, X. Lu, L. Chen, Y. Li and H. Ma, *Chem. Eng. J.*, 2024, **479**, 147882.
13 Z. Jiang, L. Wang, J. Lei, Y. Liu and J. Zhang, *Appl. Catal., B*, 2019, **241**, 367–374.
14 S. R. Nagella, R. Vijitha, B. Ramesh Naidu, K. S. V. Krishna Rao, C. Ha and K. Venkateswarlu, *Nano Energy*, 2023, **111**, 108402.
15 H. Liang, A. Wang, R. Cheng, F. Chen, P. Kannan, C. Molochas and P. Tsiakaras, *Chem. Eng. J.*, 2024, **489**, 151145.
16 Y. Li, M. Gu, X. Zhang, J. Fan, K. Lv, S. A. C. Carabineiro and F. Dong, *Mater. Today*, 2020, **41**, 270–303.
17 Y. Li, D. Zhang, J. Fan and Q. Xiang, *Chin. J. Catal.*, 2021, **42**, 627–636.
18 Q. Gu, P. P. Jiang, Y. Shen, K. Zhang, P. T. Wai and A. Haryono, *Mol. Catal.*, 2021, **504**, 111441.
19 L. Chen, X. Liu, D. Wang, Y. Xia, G. Yan, X. Huang and X. Wang, *Dalton Trans.*, 2023, **52**, 2845–2852.
20 L. Chen, H. Huang, Y. Zheng, W. Sun, Y. Zhao, P. S. Francis and X. Wang, *Dalton Trans.*, 2018, **47**, 12188–12196.
21 W. Wang, H. Zhang, S. Zhang, Y. Liu, G. Wang, C. Sun and H. Zhao, *Angew Chem. Int. Ed. Engl.*, 2019, **58**, 16644–16650.
22 X. Zhao, Y. Zhang, F. Li, Y. Wang, W. Pan and D. Y. C. Leung, *Carbon*, 2021, **179**, 42–52.
23 B. Zhu, G. Jiang, S. Chen, F. Liu, Y. Wang and C. Zhao, *Chem. Eng. J.*, 2022, **430**, 132843.
24 Z. Liu, J. Huang, B. Shao, H. Zhong, Q. Liang, Q. He, T. Wu, Y. Pan, Z. Peng, X. Yuan, Y. Liu and C. Zhao, *Chem. Eng. J.*, 2021, **426**, 130767.
25 Q. Liu, J. Shen, X. Yu, X. Yang, W. Liu, J. Yang, H. Tang, H. Xu, H. Li, Y. Li and J. Xu, *Appl. Catal., B*, 2019, **248**, 84–94.
26 P. Sun, Z. Chen, J. Zhang, G. Wu, Y. Song, Z. Miao, K. Zhong, L. Huang, Z. Mo and H. Xu, *Appl. Catal., B*, 2024, **342**, 123337.
27 G. Wu, Z. He, Q. Wang, H. Wang, Z. Wang, P. Sun, Z. Mo, H. Liu and H. Xu, *J. Mater. Sci. Technol.*, 2024, **195**, 1–8.
28 K. Huang, C. Li, X. Zhang, L. Wang, W. Wang and X. Meng, *Green Energy Environ.*, 2023, **8**, 233–245.
29 L. Chen, S. Ning, R. Liang, Y. Xia, R. Huang, G. Yan and X. Wang, *Int. J. Hydrogen Energy*, 2022, **47**, 14044–14052.
30 Z. Mo, Z. Miao, P. Yan, P. Sun, G. Wu, X. Zhu, C. Ding, Q. Zhu, Y. Lei and H. Xu, *J. Colloid Interface Sci.*, 2023, **645**, 525–532.
31 C. Hu, W. Hung, M. Wang and P. Lu, *Carbon*, 2018, **127**, 374–383.
32 A. Mohammad, P. Chandra, M. E. Khan, C. Choi and T. Yoon, *Adv. Colloid Interface Sci.*, 2023, **322**, 103048.
33 S. Wang, F. He, X. Zhao, J. Zhang, Z. Ao, H. Wu, Y. Yin, L. Shi, X. Xu, C. Zhao, S. Wang and H. Sun, *Appl. Catal., B*, 2019, **257**, 117931.
34 X. Li, J. Zhang, Y. Huo, K. Dai, S. Li and S. Chen, *Appl. Catal., B*, 2021, **280**, 119452.
35 J. Huang, D. Li, R. Li, Q. Zhang, T. Chen, H. Liu, Y. Liu, W. Lv and G. Liu, *Chem. Eng. J.*, 2019, **374**, 242–253.

36 M. Bellardita, E. I. Garcia-Lopez, G. Marci, I. Krivtsov, J. R. Garcia and L. Palmisano, *Appl. Catal., B*, 2018, **220**, 222–233.
37 F. Yi, H. Gan, H. Jin, W. Zhao, K. Zhang, H. Jin, H. Zhang, Y. Qian and J. Ma, *Sep. Purif. Technol.*, 2020, **233**, 115997.
38 Q. Zheng, D. P. Durkin, J. E. Elenewski, Y. Sun, N. A. Banek, L. Hua, H. Chen, M. J. Wagner, W. Zhang and D. Shuai, *Environ. Sci. Technol.*, 2016, **50**, 12938–12948.
39 J. Wang, L. Tang, G. Zeng, Y. Liu, Y. Zhou, Y. Deng, J. Wang and B. Peng, *ACS Sustainable Chem. Eng.*, 2017, **5**, 1062–1072.
40 Y. Yang, G. Zeng, D. Huang, C. Zhang, D. He, C. Zhou, W. Wang, W. Xiong, X. Li, B. Li, W. Dong and Y. Zhou, *Appl. Catal., B*, 2020, **272**, 118970.
41 Z. Chen, T. Fan, M. Shao, X. Yu, Q. Wu, J. Li, W. Fang and X. Yi, *Appl. Catal., B*, 2019, **242**, 40–50.
42 N. Rafique, A. H. Asif, R. A. K. Hirani, H. Wu, L. Shi, S. Zhang, S. Wang, Y. Yin, S. Wang and H. Sun, *J. Colloid Interface Sci.*, 2023, **632**, 117–128.
43 D. Guo, Y. Wang, C. Chen, J. He, M. Zhu, J. Chen and C. Zhang, *Chem. Eng. J.*, 2021, **422**, 130035.
44 G. Moon, M. Fujitsuka, S. Kim, T. Majima, X. Wang and W. Choi, *ACS Catal.*, 2017, **7**, 2886–2895.
45 S. Bach, V. R. Celinski, M. Dietzsch, M. Panthoefer, R. Bienert, F. Emmerling, J. S. A. Der Guenne and W. Tremel, *J. Am. Chem. Soc.*, 2015, **137**, 2285–2294.
46 L. E. Franken, E. J. Boekema and M. C. A. Stuart, *Adv. Sci.*, 2017, **4**, 1600476.
47 P. Moeck and P. Fraundorf, *Physics*, 2006, **2**, 533–543.
48 D. M. Zhao, C. L. Dong, B. Wang, C. Chen, Y. C. Huang, Z. D. Diao, S. Z. Li, L. J. Guo and S. H. Shen, *Adv. Mater.*, 2019, **31**, 1903545.
49 Y. P. Zhu, T. Z. Ren and Z. Y. Yuan, *ACS Appl. Mater. Interfaces*, 2015, **7**, 16850–16856.
50 K. Wang, Q. Li, B. Liu, B. Cheng, W. Ho and J. Yu, *Appl. Catal., B*, 2015, **176**, 44–52.
51 Y. Zhang, T. Mori, J. Ye and M. Antonietti, *J. Am. Chem. Soc.*, 2010, **132**, 6294–6295.
52 Q. You, Q. Zhang, M. Gu, R. Du, P. Chen, J. Huang, Y. Wang, S. Deng and G. Yu, *Chem. Eng. J.*, 2022, **431**, 133927.
53 Y. Liu, X. Wang, Q. Sun, M. Yuan, Z. Sun, S. Xia and J. Zhao, *J. Hazard. Mater.*, 2022, **424**, 127387.
54 M. Achehboune, M. Khenfouch, I. Boukhoubza, I. Derkaoui, B. M. Mothudi, I. Zorkani and A. Jorio, *Comput. Condens. Matter*, 2022, **31**, e00627.
55 X. Ma, G. Liu, L. Wang, S. Xin, B. Zhang, Q. Chen, Q. Yan, G. Zhang, Y. Zhang and Y. Xin, *J. Environ. Chem. Eng.*, 2023, **11**, 110483.
56 M. Razavi-Esfali, T. Mahvelati-Shamsabadi, H. Fattahimoghaddam and B. Lee, *Chem. Eng. J.*, 2021, **419**, 129503.
57 Y. Zeng, X. Zhan, B. Hong, Y. Xia, Y. Ding, T. Cai, K. Yin, X. Wang, L. Yang and S. Luo, *Chem. Eng. J.*, 2023, **452**, 139434.
58 S. Li, C. Wang, M. Cai, Y. Liu, K. Dong and J. Zhang, *J. Colloid Interface Sci.*, 2022, **624**, 219–232.
59 Y. Ran, Y. Cui, Y. Zhang, Y. Fang, W. Zhang, X. Yu, H. Lan and X. An, *Chem. Eng. J.*, 2022, **431**, 133348.
60 T. Zhao, D. Li, Y. Zhang and G. Chen, *J. Colloid Interface Sci.*, 2022, **628**, 966–974.
61 K. Saravanakumar and C. M. Park, *Chem. Eng. J.*, 2021, **423**, 130076.
62 R. Shen, K. He, A. Zhang, N. Li, Y. H. Ng, P. Zhang, J. Hu and X. Li, *Appl. Catal., B*, 2021, **291**, 120104.
63 O. Altan, E. Altintas, S. Alemdar and O. Metin, *Chem. Eng. J.*, 2022, **441**, 136047.